Application of dense plasma focus devices and lasers in the radiation material sciences for the goals of inertial fusion beyond ignition

View Online   Export Citation   CrossMark

V. A. Gribkov,[1,2,a] I. V. Borovitskaya,[1,b] E. V. Demina,[1,c] E. E. Kazilin,[1,d] S. V. Latyshev,[1,3,d] S. A. Maslyaev,[1,e]
V. N. Pimenov,[1,2,f] T. Laas,[2,4,g] M. Paduch,[2,5,h] and S. V. Rogozhkin[6,i]

AFFILIATIONS

[1] A.A. Baikov Institute of Metallurgy and Material Science, RAS, Leninsky Prospect 49, 119991 Moscow, Russian Federation
[2] The International Centre for Dense Magnetized Plasmas, ul. Hery 23, 01-497 Warsaw, Poland
[3] Moscow Technical University of Communications and Informatics, ul. Aviamotornaya 8a, 111024 Moscow, Russian Federation
[4] School of Natural Sciences and Health, Tallinn University, Narva Road 25, Tallinn 10120, Estonia
[5] The Institute of Plasma Physics and Laser Microfusion, ul. Hery 23, 01-497 Warsaw, Poland
[6] A.I. Alikhanov Institute for Theoretical and Experimental Physics of NRC "Kurchatov Institute", ul. Bolshaya Cheremushkinskaya 25, 117218 Moscow, Russian Federation

Note: This paper is part of the Special Issue on Materials for Inertial Fusion Reactors.
[a] Electronic mail: gribkovv@rambler.ru
[b] Electronic mail: symp@imet.ac.ru
[c] Electronic mail: elenadyom@mail.ru
[d] Electronic mail: latyshevsv@rambler.ru
[e] Author to whom correspondence should be addressed: maslyaev@mail.ru
[f] Electronic mail: pimval@mail.ru
[g] Electronic mail: tonu.laas@tlu.ee
[h] Electronic mail: marian.paduch@ipplm.pl
[i] Electronic mail: rogozhkin@itep.ru

ABSTRACT

Specimens of materials for prospective use in chambers of nuclear fusion reactors with inertial plasma confinement, namely, W, ODS steels, Eurofer 97 steel, a number of ceramics, etc., have been irradiated by dense plasma focus devices and a laser in the Q-switched mode of operation with a wide range of parameters, including some that noticeably exceeded those expected in reactors. By means of 1-ns laser interferometry and neutron measurements, the characteristics of plasma streams and fast ion beams, as well as the dynamics of their interaction with solid-state targets, have been investigated. 3D profilometry, optical and scanning electron microscopy, atomic emission spectroscopy, X-ray elemental and structural analyses, and precise weighing of specimens before and after irradiation have provided data on the roughening threshold and the susceptibility to damage of the materials under investigation. Analysis of the results, together with numerical modeling, has revealed the important role of shock waves in the damage processes. It has been shown that a so-called integral damage factor may be used only within restricted ranges of the irradiation parameters. It has also been found that in the irradiation regime with well-developed gasdynamic motion of secondary plasma, the overall amount of radiation energy is spent preferentially either on removing large masses of cool matter from the material surface or on heating a small amount of plasma to high temperature (and, consequently, imparting to it a high velocity), depending on the power flux density and characteristics of the pulsed irradiation.

I. INTRODUCTION

Radiation resistance of materials intended for the plasma-facing components (PFCs) of the chambers of nuclear fusion reactors (NFRs) with inertial plasma confinement (IPC) is an important current area of fusion research, since this resistance is essential for successful operation of future reactors of this type. PFCs are subjected to the effects of powerful and very short-pulsed blasts, and therefore, it is necessary to develop and test new types of materials that are able to withstand these conditions, with the help of appropriate simulations of IPC in NFRs.

In the context of nuclear fusion with magnetic plasma confinement (MPC) (see Ref. 1 and references therein), investigations of the corresponding problem have been carried out for several decades (see, e.g., the various Proceedings of the Symposia on Fusion Technology and of the International Conferences on Fusion Reactor Materials). In the testing of candidate materials for NFRs with MPC, quasi-stationary plasma accelerators such as QSPA Kh-50,[2,3] QSPA-T,[4] and PSI,[5] plasma guns,[6] and electron-beam heating[7] have been employed to simulate the situations in tokamaks. Heat loads are usually produced in these simulators by directed plasma streams and electron beams (thus, irradiating relatively small areas of specimens), with pulse durations ranging from a hundred microseconds to seconds. Powerful lasers operating in a free-running mode with a sequence of hundreds of pulses each 1 μs long and lasting for a total of approximately 0.1 ms can successfully simulate emergency phenomena in tokamaks, such as sawtooth instability (STI) and edge-localized modes (ELMs).[8]

As far as the second approach to nuclear fusion, namely, NFRs with IPC[9,10] is concerned, there is much less published work on radiation resistance of PFC materials. To date, most tests on these materials have used soft X rays (see, e.g., Refs. 11 and 12). However, X rays are only one source of radiation damage to chambers such as those of the National Ignition Facility (NIF)[9] and the Z Machine,[10,12] and in fact are not the most dangerous type.

The greatest threat to PFC materials in both types of NFR comes from streams of fast ions (FIS; see, e.g., Ref. 13). This is because of the considerable amount of energy that they carry during NFR operation, their short range of penetration in solid or liquid matter, the absence of a so-called "detachment" effect (which is so important for plasma irradiation), and their specific absorption mechanism with a characteristic Bragg peak at the end of their penetration path.[14] These factors result in a very high density of energy release in the bulk of irradiated material. Despite the importance of FIS, however, sources of powerful beams of fast ions such as the RHEPP-1 accelerator (Sandia National Laboratories)[15] have very rarely been used in experiments simulating damage to PFC materials.

Numerical modelling of the conditions in the NIF chamber for a direct-drive scheme and experiments performed in the hohlraum "high-foot" regime have shown that the distribution of the total of about 150 MJ of fusion energy released[9,15] is distributed among several channels (X-rays, ion and plasma streams, and neutrons) that irradiate the chamber walls.

For FIS illuminating PFCs in the NIF (about 30% of the overall energy released), the individual energy of quasiparticles E_i, the efficiency of the energy stream η, the power flux density of the irradiation stream on the target surface (i.e., on the chamber wall) P, the absorbed dose D, and the pulse duration τ expected (and already realized partially) are as follows (the NIF chamber radius is 6.5 m):[9,10,15]

- $E_i \leq$ a few MeV, $\eta \sim 30\%$, for ions of fusion origin: $P \sim 10^9$ W/cm^2, $D \sim 20$ J/cm^2, and $\tau \leq 10$ ns;
- $E_i \leq$ a few MeV, $\eta \sim 30\%$, for ions of fusion origin: $P \leq 10^8$ W/cm^2, $D \sim 20$ J/cm^2, and $\tau \leq 0.5$ μs;
- for $E_i \leq 0.5$ MeV, $\eta \sim 30\%$, for low-energy ions in the plasma formed from target debris plus ions accelerated by laser–plasma interaction: $P \leq 10^8$ W/cm^2, $D \leq 20$ J/cm^2, and $\tau \leq 3$ μs.

It can be seen from these data that IPC reactors differ from MPC reactors[1,2] in that the ion streams irradiating PFC in the former have much shorter pulse durations τ and noticeably higher power flux densities P.

At first sight, the integral damage factor (IDF)[16,17] (sometimes called the heat flux factor), given by $F = (PD)^{0.5} = P\tau^{0.5}$, may be a useful quantity for estimating the conditions on the first wall of an NFR with IPC when a long-pulse facility[2–7] is used for simulation.

Indeed, the short pulse durations in an NFR with IPC (which are in the range from 10^{-9}–10^{-6} s) may seem to be compensated by the much higher energy available in long-pulsed high-power devices, and the values of $F_{tok} = 10^8 \times (10^{-4})^{0.5} = 10^6$ W s$^{0.5}$/cm^2 for tokamaks and the corresponding simulators[1–8] and of $F_{IPC} = 10^{10} \times (10^{-8})^{0.5} = 10^6$ W s$^{0.5}$/cm^2 for NFRs with IPC[9,10] might appear to be the same. However an analysis of the relevant conditions shows that the situation is not so simple.

Generally speaking, in the various ranges of individual energies E_i of ions irradiating a target at low stream intensities, the following interaction processes will take place with the target material:

- 10^{-2}–10^1 eV: thermal activation;
- 10^{-1}–10^3 eV: desorption;
- 10^1–10^5 eV: sputtering;
- 10^2–10^7 eV: implantation.

If the power flux density of radiation P for particles having energy E_i above 10^2 eV (i.e., higher than the ionization potential) is successively increased from the implantation level of $P > 10^2$ W/cm^2 to about 10^{12} W/cm^2 and above, the radiation will have the following effects on the target material:

- implantation, i.e., an low-temperature process by which individual ions of a given element are injected into the solid material, thereby changing its physical, chemical, or electrical properties without heating it;
- heating of the target material, together with roughening, embrittlement, and cracking.
- melting, with spattering and droplet formation;
- evaporation, with droplet spraying;
- ablation of various types;
- first stage of ionization of evaporated material;
- second stage of ionization, . . .

The last three stages may be accompanied by the formation of shock waves (SWs) generated inside the irradiated target. At each stage except the first, as well as the energy expended in heating the material, some of the irradiation energy will be expended in increasing the entropy (a measure of the "devaluation of energy") of the

system—the latent heat of melting and the latent heat of evaporation—for sublimation of material (ablation), for successive stages of ionization of secondary plasma particles, for the formation of SWs, whose energy is subsequently dissipated in the bulk of the material, etc. Thus, not all of the energy (dose) of irradiation will be transformed into various forms of damage to the surface and thin subsurface layers of the target. This means that the IDF is relevant only for restricted ranges of dose or power flux density, and each case must be carefully analyzed on an individual basis.

Thus, the best situation for material testing is to use the heating methods with parameters (heat carriers and the associated individual particle energy E, dose D, power flux density P and pulse duration τ, region and mechanism of absorption, etc.) that are as close as possible to those (see, e.g., Ref. 18) that occur in real NFRs of the each type.

It should be noted that in NFRs with MCF, the conditions considered here are those associated with transients such as edge-localized modes (ELMs) or disruptions, whereas in the case of ICF, they reflect the normal operation of the facility. This means that for simulating plasma/ion bombardment fluxes in tests of materials intended for chambers with IPC, one has to use different machines from those used previously in the experiments on materials designed for PFCs of NFRs with MPC.[2–7]

Dense plasma focus (DPF) devices[19] are able to generate directed cumulative high-speed ($v_{pl} \geq 10^7$ cm/s) and dense ($n_{pl} \sim 10^{18}$ cm^{-3}) flows of hot plasma (HP), streams of fast ($E_i \geq 100$ keV to a few MeV) deuterons and tritons, fast ions of a number of materials (FIS), relativistic electrons ($E_e \geq 100$–1000 keV), and soft and hard X-ray and neutron radiation, with short (tens of nanoseconds) powerful pulses. The typical power flux densities on the surface of a target placed inside a DPF chamber are in the range $P_{pl} \sim 10^4$–10^{10} W/cm^2 for HP flows and $P_{FIS} \sim 10^6$–10^{13} W/cm^2 for FIS.

From a comparison of these heat and ion flux loads expected at the interaction of the streams with the PFC of an NFR with IPC, it can be seen that DPF facilities are very suitable for testing new materials for use in this type of NFR.

Measurements using activation and time-of-flight (TOF) techniques have shown that compact neutron sources based on medium-sized DPF devices (like Vikhr' and PF-6) are able to generate neutron intensities of ~10^9 n per pulse of duration ~10^{-8} s for a pure deuterium working gas or about 10^{11} n per ~10^{-8} s pulse for a deuterium–tritium mixture, which correspond to 10^{17} and 10^{19} n/s, respectively. On the surfaces of the compact chambers used in medium-sized DPF devices (with overall chamber areas of about $4\pi R^2 \approx 10^{-1}$ m^2), the neutron wall loading is in the range 0.1–100 MW/m^2, depending on the working gas used (D$_2$ or a D–T mixture). These figures are expected on the chamber walls of NFRs with IPC in the near future.

Facility safety issues with compact short-pulsed neutron sources based on medium-sized DPF devices with the above-mentioned neutron pulse parameters have been analyzed many times in various environments and for various regimes of DPF operation. It has been shown that at a repetition rate of about 1000 shots per day, the dose received by personnel does not exceed the permissible level at a distance $R \geq 10$ m from the source in the absence of protective screens. This is safe enough for examination (taxonomy) of modern large-sized nuclear fusion chambers of

NFRs with IPC under irradiation by neutron fluxes at the above-mentioned levels.

Solid-state Nd-glass lasers operating in the Q-switched (QS) mode may also provide heating for targets with the same power flux density and pulse duration of laser radiation (LR). This type of irradiation is of additional interest because in the NIF, LR is used as the target driver. Thus, these devices can also be used for tests of prospective materials intended for chambers of NFRs such as NIF and the Z Machine with the appropriate parameters for the heating streams.

In this context, it is important to investigate the physical processes taking place during the interactions of streams of plasma and fast ions with various targets over a wide range of power flux densities and to compare the results with those obtained for the interaction of LR with the same materials.

In general, radiation test experiments are of two types: (i) those intended to find conditions under which the first-wall materials remain unaffected and (ii) those intended to investigate different types of damage produced in environments that are similar to or even harsher than those expected during the most severe events in NFRs with IPC. Our experiments described here are of the second type.
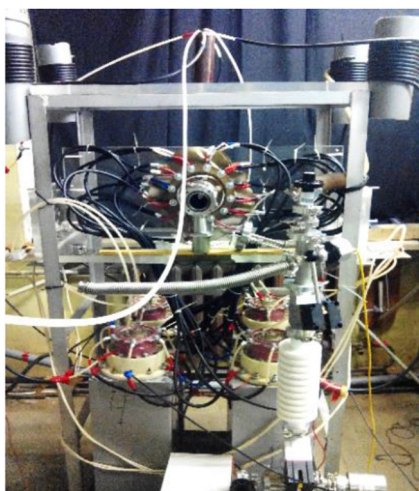
II. DEVICES

In our experiments on material testing, we used DPF devices,[20–23] as well as a Nd-glass laser working in the QS mode.[8] The DPF installations were Vikhr' (2–5 kJ) and PF-5M (2 kJ) (both at IMET RAS, Russian Federation), PF-12 (3–6 kJ) (at TU, Estonia), and PF-6 (3–7 kJ) and the large facility PF-1000U (0.2–1.0 MJ) (both at IPPLM, Poland).

The first four, relatively small, devices are capable of working at repetition rates up to 2 Hz with deuterium and with other working gases. The 1-MJ installation can produce shots every 20 min. The typical power flux densities in the DPF devices were in the ranges $P_{pl} \sim 10^4$–10^{10} W/cm^2 for plasma streams and $P_{FIS} \sim 10^6$–10^{13} W/cm^2 for fast ion fluxes. That is, at their upper levels, they noticeably exceeded the above-mentioned figures calculated and reached for the PFCs in contemporary mainstream NFRs with IPC. The Nd-glass laser that we used generated 50-ns pulses with a power flux density in the focal spot of up to 10^{12} W/cm^2.

These devices have been used previously[8,23–28] for testing materials, mostly with the power flux densities of the deuterium HP and FIS at the DPF and with the Nd-glass laser operating below 10^{11} W/cm^2. In this paper, the results of the experiments and the corresponding numerical simulations will be presented for the regimes where the above-mentioned facilities have been used with a wide range of parameters, including some that have considerably exceeded the upper levels expected in the above reactors, namely, with $P = 10^{11}$–10^{12} W/cm^2. Results will also be presented for irradiation of other materials that have been considered for possible use in the PFCs of NFRs with IPC in these modes of operation.

The investigations proceeded as follows. First, the damage to various materials produced by HP and FIS from DPF devices was investigated. Second, these effects were compared with those of laser light produced in the QS mode with similar short pulse duration and power flux density. During these tests, the DPF devices[20,22,23] (Figs. 1 and 2) were operated mainly at energy levels of $\leq$3 kJ, except for the PF-1000U facility[21] (Figs. 3 and 4), which was operated in the range 160–400 kJ. All the DPF devices used deuterium as working gas.

FIG. 1. (a) Vikhr' and (b) PF-12 devices.

In a course of the irradiation experiments, a number of important parameters, including the temporal and spatial evolutions of the density of the primary plasma (belonging to the DPF pinch and the cumulating plasma streams), the power flux characteristics of the


FIG. 2. (a) Specimen holder and (b) a specimen of tungsten attached to (c) the lid of a chamber for use in the PF-6 and Vikhr' devices.

FIG. 3. Discharge chamber of the PF-1000U facility (external view).

fast ion and relativistic electron beams irradiating the targets, and soft and hard X-ray and neutron radiation and their angular and spatial distributions, can be monitored with high temporal, spatial, and spectral resolutions. Various phenomena produced by plasma streams and FIS on the surfaces of solid targets and in the bulk of materials under test can also be observed.

Figure 2 shows a tungsten specimen fixed in a holder that can be attached to the lids of special DPF chambers of the PF-6 and Vikhr' devices. This assemblage was used in the experiments for testing the
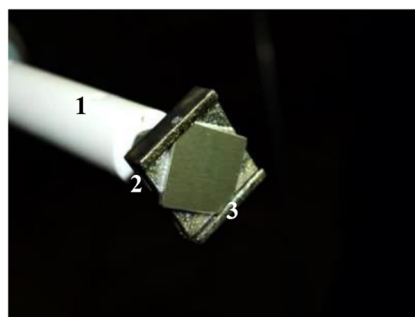
FIG. 4. (a) Virgin tungsten specimen: 1, supporting rod; 2, holder; 3, target inside the PF-1000U chamber. (b) The same specimen after irradiation.
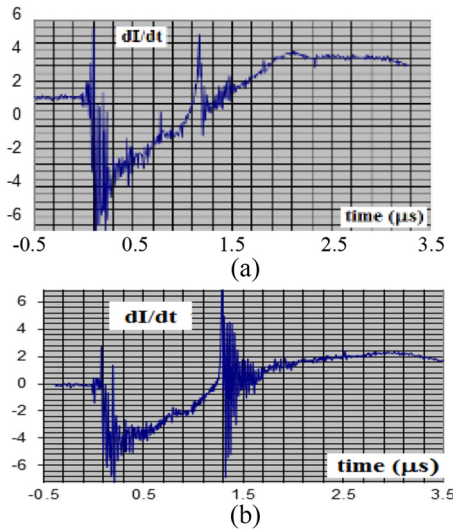
FIG. 5. Oscilloscope traces of the current derivatives of the discharges produced at the PF-6 device: (a) a "bad" shot; (b) a "good" shot.

effects on various materials of plasma streams and FIS generated in the device.

Figure 4 shows the target's assemblage placed in the cathode part of the PF-1000U facility. During some tests, the PF-1000U facility used a modified anode with a conical central insert intended to improve plasma stream formation.

The anodes of all the devices have holes in the center. These orifices prevent the powerful relativistic electron beam from evaporating the anode material (copper).
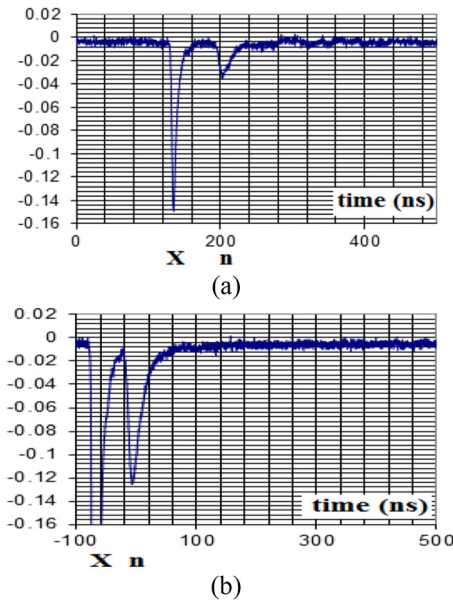

FIG. 6. PMT+S oscilloscope traces of discharges produced at the PF-6 device, with generation of hard X rays (X) and neutrons (n): (a) a "bad" shot; (b) a "good" shot.

FIG. 7. GOS-1001 laser device capable of working with a pulse of about 50 ns and 20 J in the Q-switched mode.

During operation of the DPF devices, the following parameters were monitored: the current derivative (with respect to time) by magnetic probes, the full discharge current by a Rogowski coil, and neutron and X-ray pulses by six photomultiplier tubes with scintillators (PMT+S) (the time resolution of this last technique was $\approx$2 ns). Plasma dynamics visualization was provided by time-integrated photography in the visual range, by 1-ns four-frame self-luminescence registration, and by 16-frame laser interferometry (1 ns for each frame with time intervals of 20 ns or 30 ns between them). The absolute neutron yield was monitored using Ag, In, Y, and Be activation counters.

After a number of conditioning discharges of the DPF devices, they started to generate neutrons and hard X rays. Measurement of the current derivative of a discharge and of absolute neutron yield generated by the device gave data on the strength of the particular discharge ("shot").

Usually the current derivative is measured by a magnetic probe, whereas the neutron yield in a DPF is determined by two methods, namely, from data obtained with activation counters and by examination of oscilloscope traces of a time-resolved fast probe. The "quality" of the discharge and the power of the ion beam in each DPF device were estimated from the sharpness and amplitude of the current derivative peak on oscilloscope traces (Fig. 5) as well as from the amplitude of the corresponding neutron flash (Fig. 6) plus the absolute neutron yield measured by activation techniques.

A single-cascade laser device, GOS-1001,[8] with a flat resonator (Fig. 7) capable of working in the QS mode (ensuring values of $P = 10^9$–10^{12} W/cm^2, $\tau = 50$ ns) was used for heating of targets by LR in the regime with parameters close to those typical of the FIS generated in the PF-6 and Vikhr' devices.

III. MATERIALS, IRRADIATION CONDITIONS, AND ANALYSIS TECHNIQUES

At present, it is rather difficult to make a final choice in favor of a preferred material for use in the PFCs of NFRs with IPC. This is because the interactions of FIS and LR with chamber walls under the conditions within these reactors are not completely known (see some results on this point later in this paper). An intensive search for new materials is in progress. The types of material that must be tested for reliable and efficient implementation in inertial nuclear fusion chambers include both conventional (solid metallic) materials and liquid metals used as an alternative PFC concept. All such material must be able to withstand high power loads at high wall temperatures. The aim of the tests is to find materials that are resistant to heating by powerful short-pulse heat and particle loads, that have long lifetimes (exhibiting endurance under erosion and material mixing, as well as retention of stable surface morphology), and that allow safe

operations (with regard to fuel retention and removal, material migration, and dust formation).

The list of candidate materials includes the following: tungsten and other highly refractory metals (e.g., Mo and V), their alloys and coatings, high-entropy alloys (e.g., FeNiMnCr, WTaVCr, VCrTi, and VCrTiY), reduced-activation ferritic–martensitic (RAFM) steels, oxide-dispersion-strengthened ferritic or ferritic–martensitic steels and other metals reinforced by TiO_2, ZnO, Nb_2O_5, and CuO (ODS steels), and various ceramics [e.g., carbon fiber composites (CFCs), SiC, and Al_2O_3]. Nanostructured W and SiC (as a tritium barrier and an anticorrosion cover), diamond-like carbon (DLC), N_3Ti, AISI 316L and ASP 30 steels, W with 25% Re (W25Re), and 1% TiC in W (W–TiC) are also under intensive testing at present.

As optical materials tested for use in the first wall (windows for laser beams and for diagnostics, i.e., in the final optics), quartz, synthetic diamonds, sapphire and leucosapphire (Al_2O_3), CaF_2, MgF_2, KS-4V glass, and various multilayer nanoparticle armoring materials have been examined.

Candidate wet materials with a thin liquid layer or with thick liquid protection for sweating walls of NFRs include Pb, Li17Pb83 eutectics, Li_2BeF_4, and alloys of the type 01 420 Al–Mg–Li.

A variety of dissimilar materials for application in the construction of NFRs (Al, Ti, ceramics, etc.) also have to be examined under direct irradiation because their exposure to high energy loads could lead to possible damage or even to PFCs inside the NFR chamber becoming detached.

In this study, the materials under test were as follows:

- double-forged tungsten;[29]
- ODS steel: Fe–15Cr–4Al–2W–0.35Y_2O_3 ferritic steel KP4-ODS (Kyoto University) (which is thus different from the Fe–16 Cr–4Al–2W–0.3Ti–0.3Y_2O_3 ODS steel investigated in Ref. 27);
- Eurofer 97 stainless steel;
- V–10Ti–6Cr alloy;
- several types of specialized ceramics.

These materials are all considered to show promise for use in the PFCs of NFRs with IPC because of their good resistance to radiation and to shock-like impacts.

As mentioned above, DPF devices are particularly suitable for experimental tests of materials for use in NFRs with IPC because these devices can generate directed streams of particles with energies (individual ion energies in the range 1.0 keV to a few MeV) and power flux densities ($P \sim 10^6$–10^{12} W/cm^2) similar to those observed on the chamber walls of such NFRs. The laser pulses of the GOS-1001 device used in its QS mode can also simulate conditions occurring in NFRs with IPC. However, because the mechanisms and zones of absorption of laser energy and of particle streams from DPF devices are different, it is important to compare the results of irradiation of materials by these two types of beams (LR and HP/FIS) with similar parameters.

In the tests in the DPFs described here, the specimens were usually placed on the Z axis of the DPF chamber with their flat surface perpendicular to this axis at various distances from the DPF anode (see the photographs in Figs. 2 and 4 and the diagram in Fig. 8). In the PF-1000U and PF-12 facilities, these distances were 7 cm, 11.5 cm, 30 cm, and 50 cm, whereas in the PF-6 and Vikhr' devices, they ranged from 3.4 cm to 18 cm.
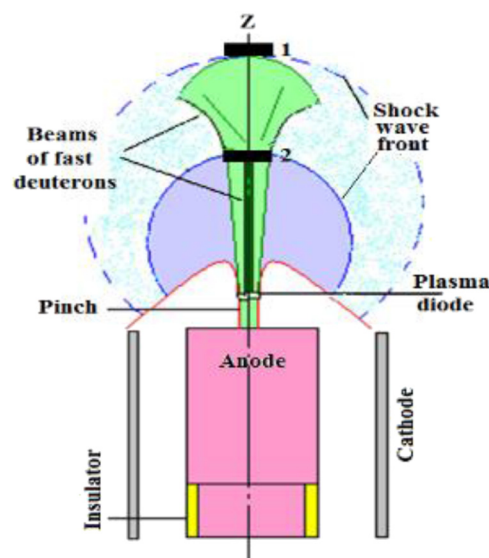
FIG. 8. Schematic of a hot plasma stream with a shock wave pushing past it and fast ion streams spreading into space from the DPF anode and irradiating targets placed at two positions (1 and 2).

The minimum distance from anode to specimen ensures almost the same maximum power flux density in all DPF devices, although in the medium-sized DPFs, this is spread over a much smaller area. The specimen holders were constructed in such a way that the specimen surface was maximally protected from any redeposition of holder material (Figs. 2 and 4). Each specimen was subjected to 1, 2, 4, 8, and 16 up to 50 consecutive shots. The power flux densities of the plasma stream and FIS could be tuned by changing the distance between the top of the pinch and the target under irradiation.

Experiments on interaction of LR with materials were performed in air and in vacuum by using the GOS-1001 laser in the QS mode according to the scheme shown in Fig. 9. This regime was realized with the maximal parameters $P_{LR} \approx 10^{12}$ W/cm^2, pulse duration 50 ns, and focal spot diameter $d \le 0.1$ mm. Reductions in the power flux density of LR were accomplished by defocusing.
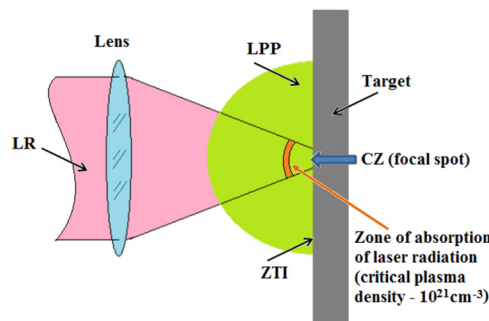
FIG. 9. Scheme for investigating the action of LR on a target using a laser working in the QS mode: CZ, central zone of LR (the focal spot); ZTI, zone of thermal influence of the laser-produced plasma (LPP).

From interferometric images (with a 1-ns time exposure of each frame and time intervals of 20 ns or 30 ns between the 16 frames), it is possible to measure the characteristics of hot plasma streams of primary plasma (the "pinch plasma") in the device (Fig. 10). Indeed, the interferometric images display the dynamics of plasma density and shape both for the upper part of the current sheath (pinch, CS) and for the cumulative stream propagating along the Z axis that is collected near the target surface. Thus, we obtain the necessary characteristics of the primary plasma (deuterium) cumulative stream driven onto a target.

The interferometric image in Fig. 11, taken at a later time than the image in Fig. 10, gives an opportunity to measure the speed of the secondary plasma (SP) from a stainless steel target created near the target surfaces by a powerful FIS and propagating in the direction toward the anode.

In a previous paper,[28] it was shown that the velocity of the edge of a freely expanding hot SP (from the target) can be measured from such interferometric pictures. This velocity is related to the initial SP temperature T_{SP}. Thus, these measurements allow the extraction of important characteristics (namely, n_e and T) of the SP for each material under irradiation. It is essential to mention here that interferometric plasma images of later stages in regions close to the target when the secondary plasma is well developed cannot be processed for two reasons: first, the interferometric fringes are too condensed and consequently cannot be distinguished from each other; second, for high-Z materials (e.g., tungsten), the SP at the estimated temperature (≈ 50 eV) is not transparent to the second harmonic of the diagnostic Nd-glass laser light.

Neutron pulses in a DPF give information on the parameters of FIS in a DPF. In a previous study (see Fig. 7 of Ref. 28), it was shown that the mass loss from a target (which is governed mainly by the powerful FIS) is linearly proportional to the neutron yield. Actually, because neutrons in a DPF are produced by a beam–target mechanism, the neutron yield in a shot is given by the formula

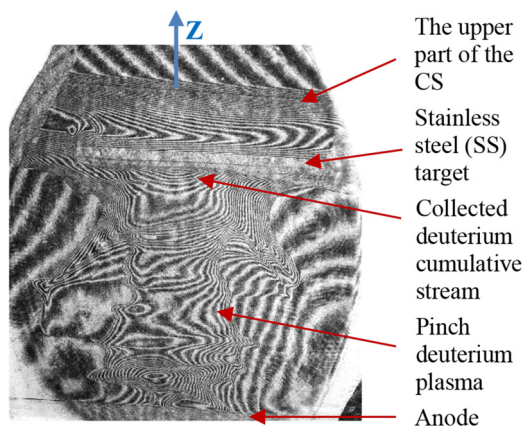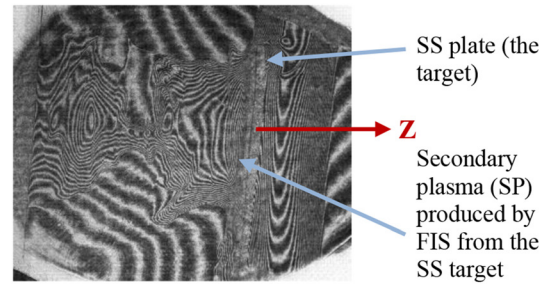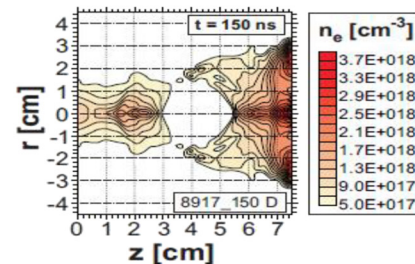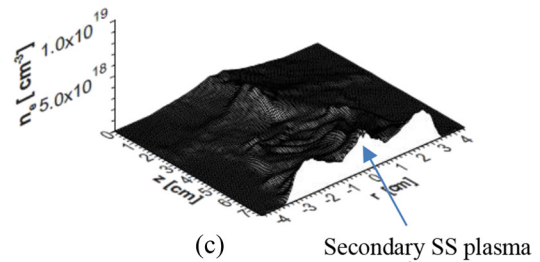$$Y_n = \frac{n_{pl} N_{i\,fast}}{4} \sigma v_{i\,fast} \pi R_p^2 h_p \tau, \tag{1}$$

FIG. 10. Interferometric picture of a pinch with the upper part of the current sheath (CS) and a stainless steel plate with plasma from a cumulative stream collected in front of it.
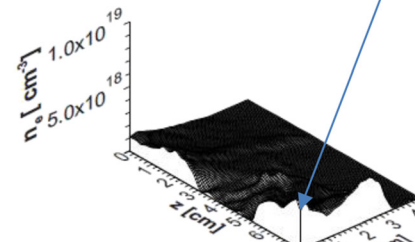

FIG. 11. (a) Interferometric image, (b) contours of electron density, and (c) and (d) the 3D electron density distribution. The secondary plasma can be seen to be propagating from the target ($Z = 8$ cm) toward the anode ($Z = 0$).

where n_{pl} is the density of the plasma in the pinch, and $N_{i\,fast}$ is the concentration of fast ions in the pinch (with velocity $v_{i\,fast}$), which is approximately equal to the overall number of fast ions. This yield gives data on the FIS power. For the PF-1000U facility, the relevant parameters are a pinch length $h_p \approx 10$ cm, a pinch cross-sectional area $R_p^2 \approx 1$ cm^2, the velocity $v_{FIS} \approx 3 \times 10^8$ cm/s of fast deuterons with mean energy of about 100 keV in the DPF, the pulse duration $\tau_{FIS} \approx 40$ ns of fast deuterons, and the cross-section of the fusion reaction for fast (~100 keV) deuterons. The absolute neutron yield is thus

proportional to the power flux density of the fast ion stream, and so both of the powerful streams (HP and FIS) can be monitored by the above two techniques.

A number of analytical methods were used to investigate specimens [both their surface layers (SLs) and the bulk materials in metallographic sections] before and after irradiation. This yielded information on changes in the elemental and molecular contents, structure, and properties of irradiated materials.

Among these methods, classical optical and scanning electron microscopy as well as atomic emission spectroscopy (AES) (with a LECO SA-2000 glow discharge spectrometer) were used to determine the character and parameters of damage to specimen SLs and to the bulk material (using an EVO 40 microanalyzer). Atomic force microscopy was used to measure specimen surface roughness after irradiation. A tomographic atom probe was implemented for investigation of oxide particles in the irradiated ODS steels and Eurofer 97 stainless steel. X-ray structural and elemental analysis, weighing of specimens, and measurements of their micro- and nanohardness were performed before and after irradiation.

We shall present here some new results obtained by these techniques when applied to the various materials from different classes that were used as targets for irradiation in DPF devices by HP and FIS, as well as by LR.

IV. INVESTIGATIONS OF THE PHYSICAL PROCESSES OF PLASMA–WALL INTERACTION OCCURRING ON IRRADIATION OF DIFFERENT MATERIALS

Measurements of the SP maximum velocities V_{MAX} observed at the beginning of the propagation of the SP cloud from targets made from three types of materials (W, Eurofer 97 stainless steel, and SiC) gave the values shown in Fig. 12. It can be seen that the asymptotic speeds of the SP clouds depend linearly on the atomic mass of the irradiated elements. Using these data, one can estimate the
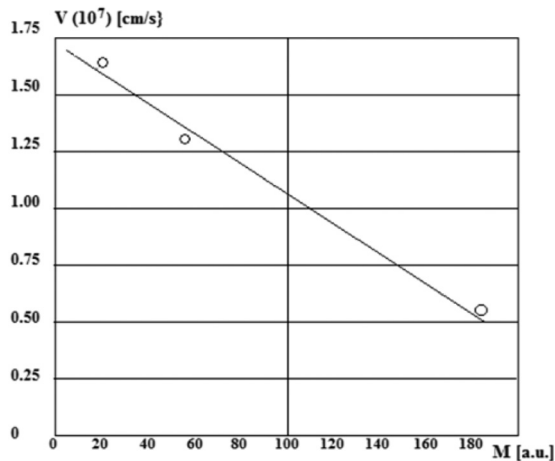

FIG. 12. Experimentally obtained propagation speed of SP from the target in the direction toward the anode as a function of atomic mass for three different materials (W, stainless steel, and SiC) irradiated under the similar conditions ($P_{FIS} \approx 10^{12}$ W/cm^2) in the PF-1000U facility.

temperatures of the SP clouds. Rough approximations can be obtained with a help of the adiabatic law given in Ref. 30 for the free spherical expansion of an ideal gas into vacuum:

$$V_{MAX} = \frac{2}{\gamma - 1} V_S, \qquad (2)$$

where V_{MAX} is the maximum (asymptotic) velocity of the expansion of the front part of the plasma at the end of the irradiation by the FIS irradiation, and $\gamma = 5/3$ is the isentropic exponent. V_S is the sound velocity calculated according to the formula:

$$V_S = \left[\frac{\frac{5}{3}(Z+1)kT}{m} \right]^{1/2}, \qquad (3)$$

where T is the plasma temperature and Z is the mean ionic charge, both at the moment of maximum intensity of FIS. In this case, the sound velocity is one-third of the asymptotic speed of the gas.

However, more accurate numerical simulations of the interaction have been performed in this case for two values of the power flux density of FIS ($P_{FIS} = 10^{11}$ and 10^{12} W/cm^2) and for two durations of the FIS pulse ($\tau = 20$ ns and 50 ns at the base of the pulse), with the use of the software described in Refs. 31 and 32. The shape of the heating pulse of the FIS was taken as a half-sinusoid:

$$P(t) = P\sin(\pi t / \tau). \qquad (4)$$

The focal spot of the FIS striking the target surface was $d = 1$ mm. The results obtained are presented in Table I.

It can be seen that the maximum velocity of expansion of the front part of the plasma bunch at the end of the irradiation by the FIS, V_{MAX} is higher than the sound velocity V_S by a factor of 1.5–2.5 times, in contrast to the factor of 3 times claimed in Ref. 30.

This is because, after the end of irradiation by the FIS, there is heat transfer from the plasma to the target contrary to the adiabatic law.

Table I demonstrates also that the experimental data on the speed of the SP are better fitted to the simulation results obtained for $P = 10^{12}$ W/cm^2 (and thus for the highest power flux densities of FIS used in the real experiment) with $\tau = 20$ ns (for W) and $\tau = 50$ ns (for Fe and SiC).

This fact that dissimilar pulse durations fit the experimental data for dissimilar materials can be connected to a certain spread of data in the DPF operation and with the fact that the simulations were performed in the last case for pure Si, rather than not for the material actually used as a specimen, namely, SiC.

V. RESULTS AND DISCUSSION

A. Irradiation of W specimens at low P resulted in roughening and spattering

We started with low-power irradiation with HP and FIS, using relatively low power flux densities $P = 50$ MW/cm$^2 = 5 \times 10^7$ W/cm^2 and $P = 500$ MW/cm$^2 = 5 \times 10^8$ W/cm^2. At the distances from the anode used in the experiments with the PF-12 device, the power flux densities of these streams were approximately equal and were lower than those to be expected in NFRs with IPC. % Fe and 2 wt. % Ni) and HPM1810 (W with 1.67 wt. % Fe, 3.33 wt. % Ni, and small amounts of Co and Cu in a binder phase). In this case, we tried to find the roughening threshold with no melting of the material. 3D profilometry was carried out

TABLE I. Results of a numerical simulation of SP propagation for three materials and under dissimilar irradiation conditions.

P (W/cm^2)	τ (ns)	T (eV)	Z	V_{MAX} (10^6 cm/s)	V_S (10^6 cm/s)	$V_{MAX\,EXP}$ (10^6 cm/s)
			W			
10^{11}	20	24	7.1	1.9	1.3	
10^{11}	50	28	9.4	2.6	1.6	
10^{12}	20	52	15	5.7	2.8	5.6
10^{12}	50	54	17	7.7	3.0	
			Fe			
10^{11}	20	20	5.4	3.3	2.0	
10^{11}	50	26	8.3	4.7	2.7	
10^{12}	20	50	12	9.8	4.5	
10^{12}	50	53	14	13	4.8	13
			Si			
10^{11}	20	28	5.3	6.7	3.2	
10^{11}	50	28	6.3	8.4	3.5	
10^{12}	20	50	10	14	5.7	
10^{12}	50	51	11	15	6.0	17 (for SiC)

on a Bruker Contour GT-K0+ 3D white light optical microscope (with vertical resolution <0.01 nm, lateral resolution 0.38 μm, and single-image resolution 1280 × 960 pixels). This instrument also allowed us to estimate the 3D microroughness parameters averaged over five measurements of the investigated surface. The data included in the current study are the arithmetic mean surface roughness R_a of the height distribution and the total height R_t of the roughness profile.

After 25 shots, only an increase in microroughness and slight sputtering of the surface were observed (Fig. 13). This result for the DF tungsten specimens is in good agreement with data on the roughening threshold for W (about 1 J/cm^2) obtained with an ion beam from the RHEPP-1 device[15] with slightly different parameters to the FIS pulse: 800-keV He ions, pulse width 100–300 ns, and <250 A/cm^2.

The main result of the present experiments (besides the roughness threshold) was that the change in power flux densities P of HP and FIS within a range of one order of magnitude (on a threefold change in the distance to the target) was less important for roughness creation (with a change from $R_{a0} = 0.9446$ μm to $R_a = 1.87$ μm, i.e., by a factor of just 2) than the number of irradiating shots (a change from 25 shots to 100 shots gave $R_a = 5.12$ μm: an increase by a factor of more than 5 compared with the unirradiated specimen).

B. Irradiation of W specimens at high P resulted in melting and large changes in morphology

In our previous work,[28] when we increased the power flux density to $P \approx 10^{11}$ W/cm^2 and irradiated double-folded specimens of tungsten with shorter distances between the DPF anode and the target, a number of unexpected results were obtained. (1) The deuterium concentration inside the irradiated material decreased with increasing number of DPF shots. (2) There was a disproportionality in the amount of mass evaporated with respect to the increase in P (under the conditions of well-developed gasdynamic motion of the SP). (3) A remarkably lower mass was removed from ceramic (thermally insulating) materials at higher flux

(a)

(b)
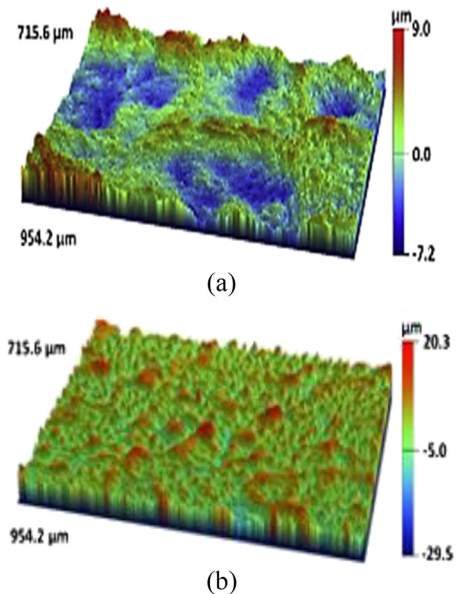
FIG. 13. Microroughness of W alloy specimens irradiated at the PF-12 device: (a) 25 shots and power flux density P = 500 MW/cm^2, giving R_a = 1.87 μm; (b) 100 shots and power flux density P = 50 MW/cm^2, giving R_a = 5.12 μm.

densities compared with tungsten (a material with a significant thermal conductivity). These results were explained by changes in the morphology of the irradiated surface layer, by the effect of redistribution of the pulsed energy among the large mass of low-temperature material evaporated at low P and the low mass of high-temperature material evaporated at higher P, and by the absence of thermal conductivity effects in the case of very short pulses (with durations negligible compared with the time scales characteristic of heat conduction).

In the present experiments, when the power flux density was increased by an additional order of magnitude to $P \approx 10^{12}-10^{13} \, W/cm^2$, the results obtained supported these explanations (Fig. 14). It can be seen that the SLs acquire much higher surface area, sometimes
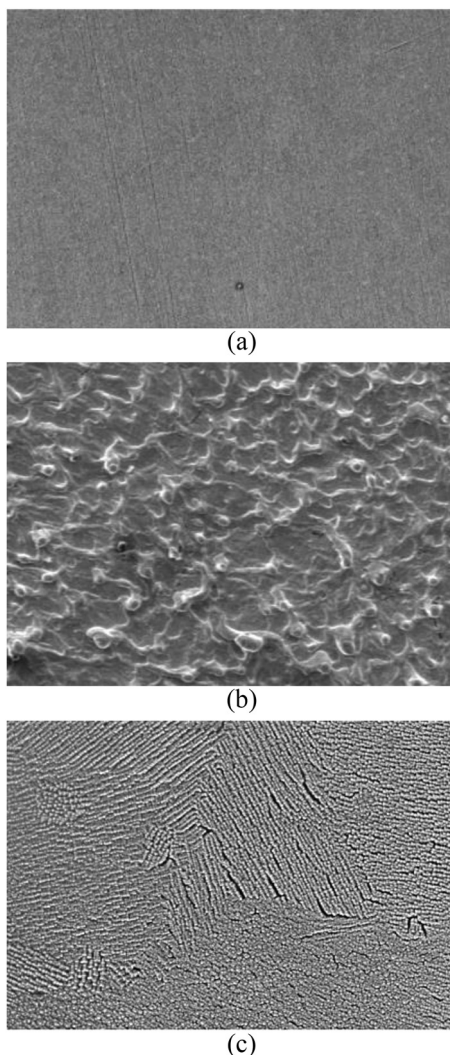
FIG. 14. SEM images of double-forged W specimens (a) before irradiation and after several shots from a DPF in regimes with (b) high and (c) very high power flux density P_{FIS}.

nanostructured [Figs. 14(b) and 14(c)]. Thus, the outward gas diffusion of deuterium from the specimens into the chamber becomes much easier in this case.

In the well-developed gasdynamic motion of the SP bunch that occurs at the high power flux density $P \approx 10^{12} \, W/cm^2$ of FIS or LR produced during a short pulse (shorter than the characteristic time for spread of the SP bunch), the plasma temperature becomes very high, and energy and momentum conservation dictate that the variables M (mass of the evaporated material) and T (its temperature) must be in a linear relationship: the higher the value of T during irradiation (i.e., the higher the power flux density of the streams), the lower will be the mass M that is evaporated.

At the same time, it is clear that when the heating pulse is short compared with the characteristic heat conduction time, the role of the thermal conductivity of the material becomes negligible. That is why our five ceramics under test (Al_2O_3, CFC, SiC, ZrB_2–SiC–Si_3N_4, and HfB_2–SiC) all lost mass under irradiation by short pulses of FIS at the same level or even lower (1–2 mg after only six pulses) than the tungsten specimens (up to 6 mg with six pulses).

On the basis of these result, one can calculate a duty cycle for each material. For example, for double-forged tungsten, the thickness of the layer removed from the specimen by a single powerful shot from a DPF with $P \sim 10^{12} \, W/cm^2$ appeared to be about 0.5 μm.

C. Irradiation of ODS steels

1. Introduction

Among the alternative materials considered for use in PFCs of NFRs with IPC are oxide-dispersion-strengthened (ODS) ferritic and ferritic–martensitic steels.[27,33–38] They have enhanced mechanical characteristics at high temperatures (>700 °C) as a result of their high content of dispersed inclusions of oxide particles (Y_2O_3, Al_2O_3, TiO_2, etc.) of nanoscale sizes. These prevent movement of dislocations and consequently help to increase the stability of grain-restricted structures and their resistance to creep.[39,40]

The radiation resistance of ODS steels results from the behavior of the dispersed structure and mainly because of the stability of the oxide nanoparticles under prolonged irradiation by streams of high-energy particles and various other forms of radiation. It is hoped that in ODS steels, the high density of oxide nanoparticles, which are centers for the capture and annihilation of point defects, will ensure a low level of vacancy swelling and preserve stability of the nanoparticles under the levels of irradiation to which PFCs in NFRs with IPC are subjected.

However, in a number of preliminary experiments, it has been shown that irradiation of ODS steels may result in degradation of their mechanical and radiation properties. For example, intense low-temperature embrittlement and a loss of plasticity were observed in specimens of the ODS Eurofer at low doses of neutron irradiation (<10 dpa).[41,42]

Irradiation of ODS steels by heavy ions and by fast neutrons at high dose (81 dpa) has led to loss of stability of the oxide nanoparticles, possible radiation dilution, and changes in elemental composition. That is why investigations of the effects of pulsed radiation on ODS steels using DPF devices are important for evaluating these materials for potential applications in NFRs with IPC.

TABLE II. Irradiation conditions for ODS steel specimens in the PF-1000U device.

Specimen no.	Average power flux density of HP stream, P_{HP} (W/cm^2)	Average power flux density of FIS, P_{FIS} (W/cm^2)	Number of irradiation pulses, N	Aggregate neutron yield, number of G–M counts	Distance from target to anode, L (cm)	Irradiation time (ns) FIS	Irradiation time (ns) HP
3	10^8	10^9	2	10 827	50	50	100
2	10^8	5×10^9	9	85 567	50	50	100

2. Irradiation conditions, materials, and methods of analysis

In the experiments described here, irradiation of specimens of ODS steels having a high concentration of chromium were carried out with the PF-1000U device operating at a bank energy of ~170 kJ (charging voltage 16 kV), with pure deuterium as working gas at an initial pressure p_0 = 470 Pa.

Two specimens of the ODS ferritic steel KP4-ODS (Kyoto University) with composition Fe–15Cr–4Al–2W–0.35Y$_2$O$_3$ and dimensions 12 × 12 mm^2 were irradiated: No. 3 specimen by two pulses and No. 2 specimen by nine pulses. The distance between the DPF

(a)

(b)
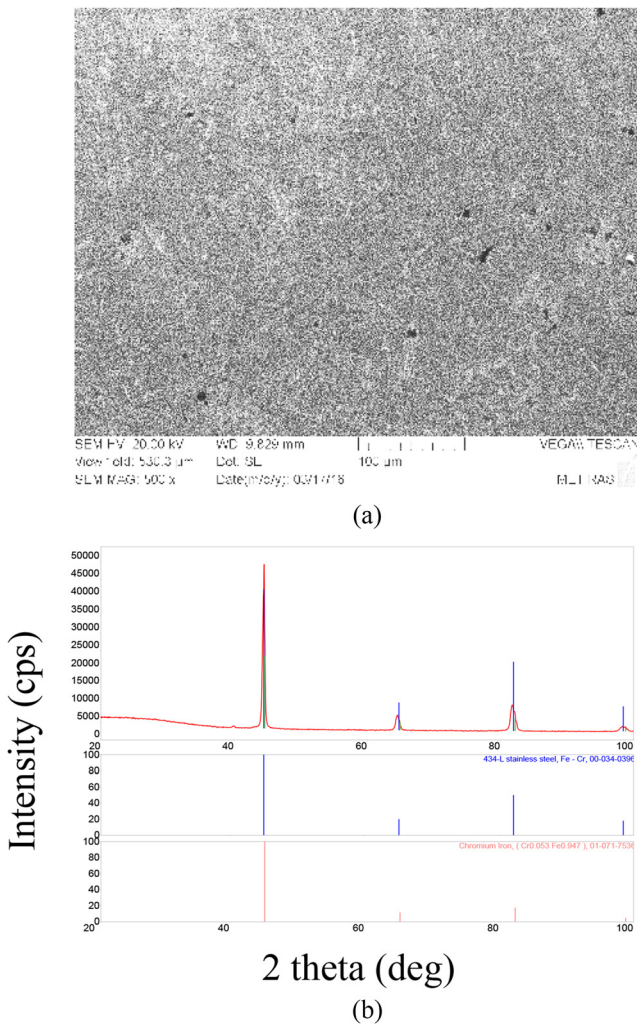
FIG. 15. (a) Microstructure (SEM) and (b) X-ray diffraction pattern of an unirradiated polished specimen of KP4-ODS steel.
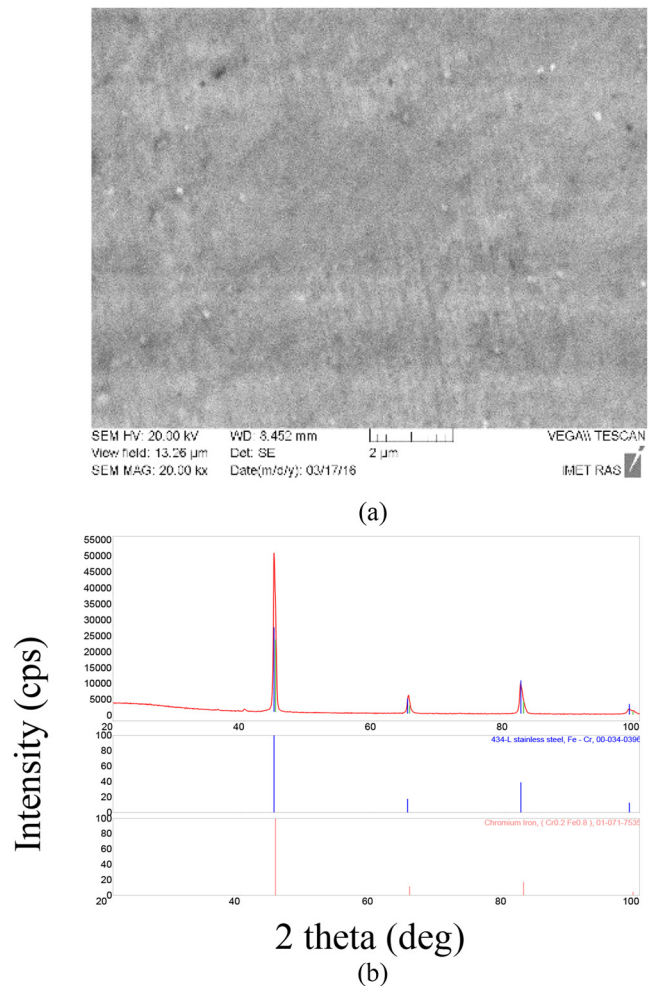

(a)

(b)

FIG. 16. (a) Microstructure (SEM) and (b) X-ray diffraction pattern of a specimen of KP4-ODS steel irradiated with pulsed streams of deuterium ions and deuterium plasma (N = 2).
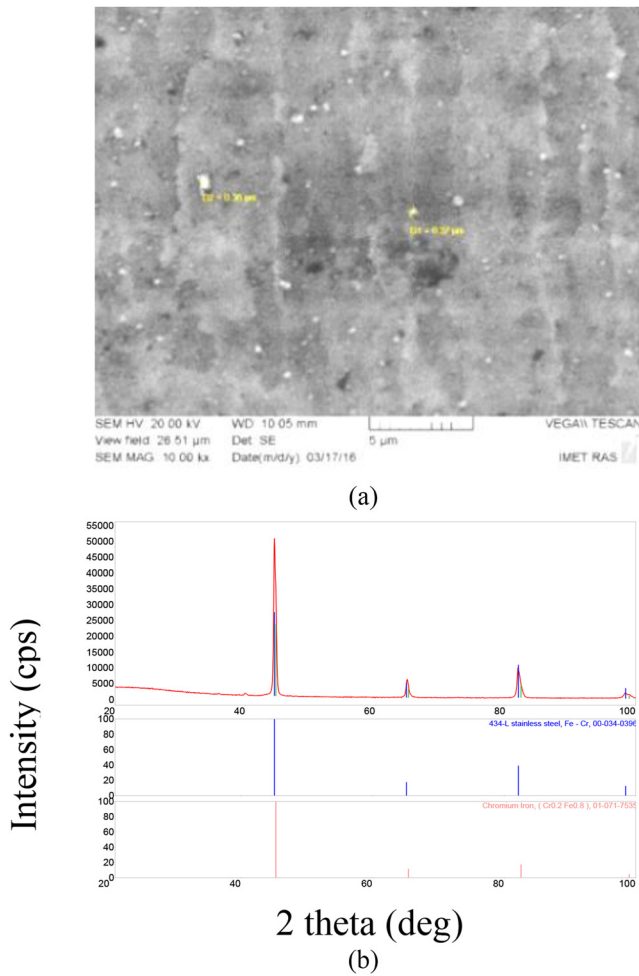
(a)

(b)

FIG. 17. (a) Microstructure (SEM) and (b) X-ray diffraction pattern of a specimen of KP4-ODS steel irradiated with pulsed streams of deuterium ions and deuterium plasma ($N = 9$).

anode and the specimens was $L = 50$ cm. Table II shows the irradiation conditions.

Besides the above-mentioned analytical techniques, the specimens were investigated by means of tapping-mode (atomic force) microscopy (AFM). The analysis was performed in two zones

(5 and 6). The image dimensions were 20×20 and $5 \times 5 \ \mu m^2$. For the same area on each specimen, regions of dimensions 1×1, 10×10 and $50 \times 50 \ \mu m^2$ were examined.

3. Results and discussion

a. Microstructure of the surface layer. Figures 15–17 show SEM images of the microstructures of virgin and irradiated ODS steel specimens taken after the experiments, together with their X-ray diffraction patterns.

It is almost impossible to find changes in the microstructure of the specimen irradiated by two pulses compared with the virgin one, except that there is a greater degree of micro-inhomogeneity on the surface of the latter [compare Figs. 15(a) and 16(a)].

From a comparison of the values of the mean roughness parameter R_a (Table III), it can be concluded that after a double irradiation, the initial roughness of the ODS specimen SL becomes smoother, although the parameter R_{max} remains almost unchanged.

However, in the experiments carried out with nine pulses and at a higher power flux density, melting of the SL is evident (Fig. 17). The presence of the melt on the surface of the ODS steel specimen here is also evidenced by a noticeable increase in the extractions of the second phase observed in Fig. 17. These extractions show themselves as white particles of sizes in the range 10–100 nm. Very likely, they are formed during the solidification stage. These data are consistent with the results of investigations of the topographical structure of ODS steel specimens by AFM in their initial state and after irradiation in a DPF that are presented in Fig. 18 and Table III.

From a comparison of the values of the mean roughness parameter R_a for the specimens under investigation (Table III), it can again be concluded that after the twofold irradiation, the initial surface imperfections of the ODS steel specimen became smoother, although the maximum difference in the zones under analysis (the parameter R_{max}) remained practically unchanged.

However, after the ninefold irradiation, both parameters were increased by a factor of about two compared with the virgin specimen.

This supports the above-mentioned result on melting of the SL and creation of wave-like reliefs. It is quite typical for materials irradiated in a DPF device.[24–28] The ninefold irradiation also led to the very large increase in the second phase extraction that can be seen in Figs. 17 and 18 and that appeared as a rule during the cooling stage. Analysis of the X-ray diffraction patterns indicates the presence of two solid solutions within the ODS steel specimens. The virgin specimen composition has 95% of the phase enriched by Fe (with lattice parameter $a_{Fe} = 2.8823$ Å) and 5% of the phase enriched by Cr ($a_{Cr} = 2.8724$ Å).

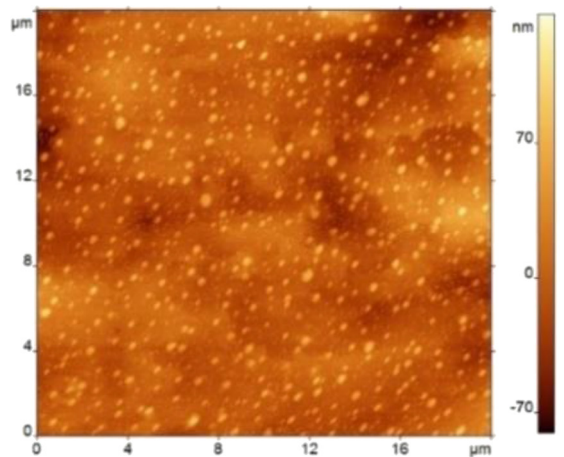**TABLE III.** Surface roughness parameters of specimens of KP4-ODS steel.

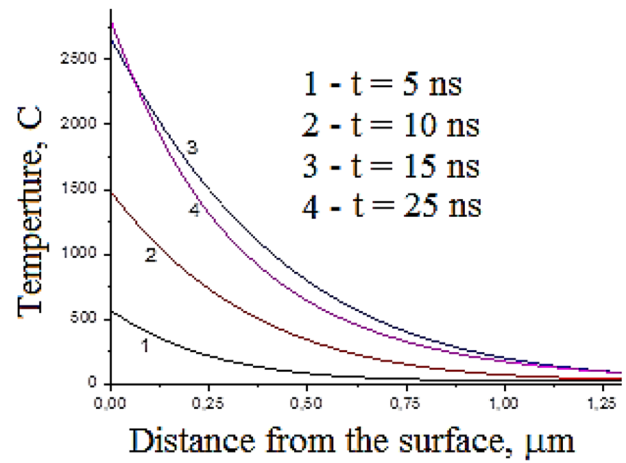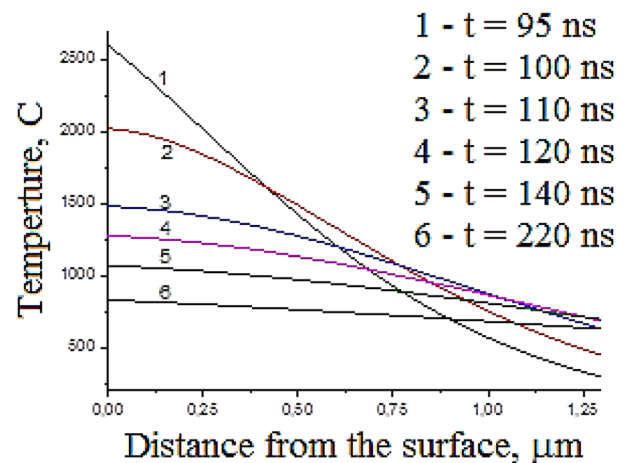|	Image size			
	$5 \times 5 \ \mu m^2$		$20 \times 20 \ \mu m$	
Specimen	R_a (nm)	R_{max} (nm)	R_a (nm)	R_{max} (nm)
Virgin	5.9 ± 1.2	34 ± 5	9.4 ± 0.9	75 ± 15
Irradiated, $N = 2$	5.5 ± 1.1	38 ± 7	7.8 ± 1.0	74 ± 8
Irradiated, $N = 9$	13 ± 2	78 ± 2	19 ± 5	133 ± 20
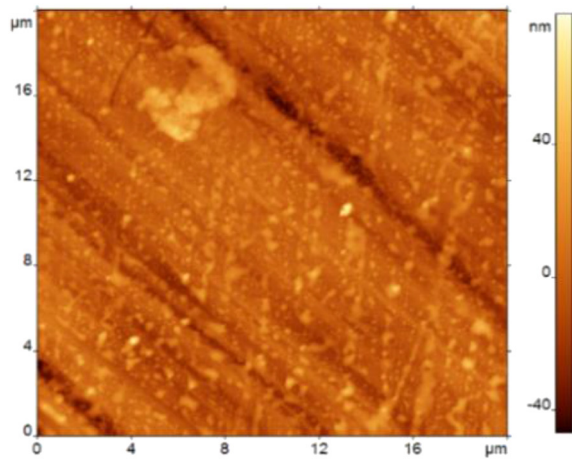
(a)
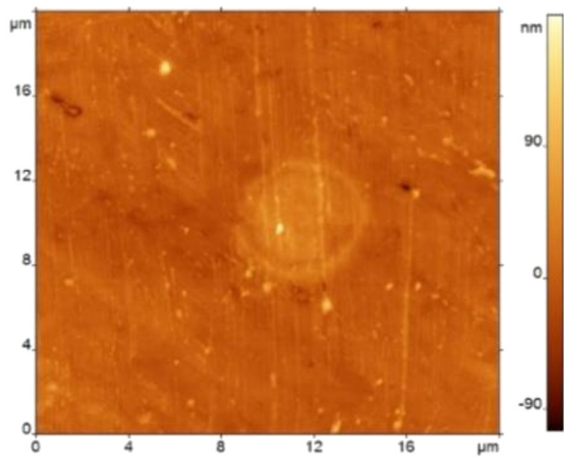
(b)

(c)

FIG. 18. AFM images of the surface of a specimen of KP4-ODS steel (a) in the initial state and after irradiation with (b) two and (c) nine pulsed fluxes of deuterium ions and deuterium plasma.
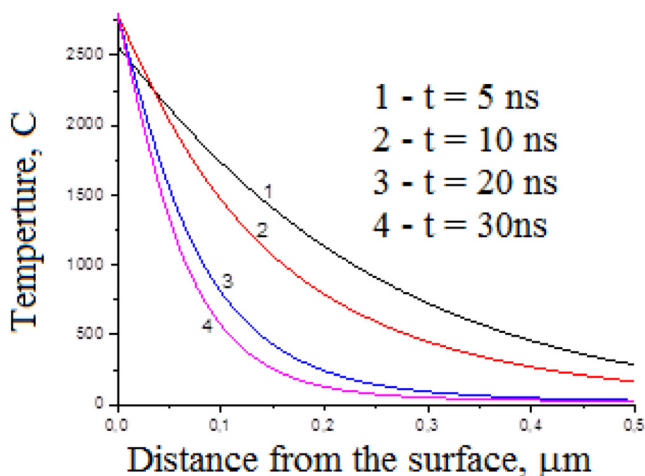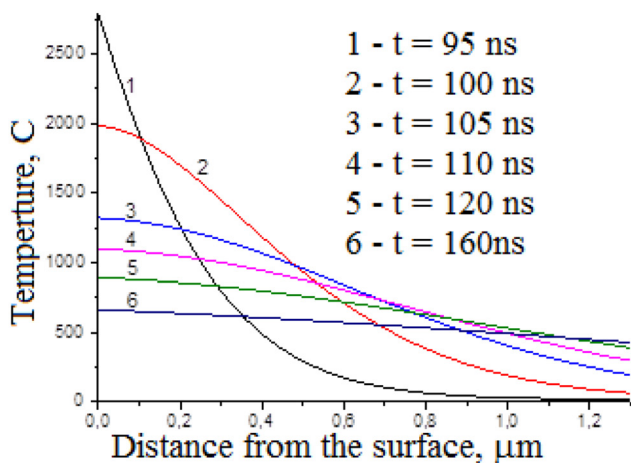

(a)

(b)

FIG. 19. Temperature distributions over the depth of the SL of a KP4-ODS steel specimen at various times (a) when it was heated by fluxes of fast deuterons and HP in the soft irradiation mode ($P_{FIS} = 10^9$ W/cm^2, $\tau_{FIS} = 50$ ns; $P_{HP} = 10^8$ W/cm^2, $\tau_{HP} = 100$ ns) and (b) upon cooling.

In the specimen irradiated by two pulses, the phase composition was preserved, although the lattice parameters were changed: for the Fe-based solution, a_{Fe} decreased to 2.8678 Å, whereas for the Cr-based solution a_{Cr} increased to 2.8779 Å. These changes are related to redistribution of elements due to evaporation and to redeposition of functional elements of the discharge chamber.

In the specimen that was irradiated by nine pulses with higher power flux density (see Table III), the SL melted, resulting in a change in phase composition. The Cr-based phase disappeared owing to stronger diffusion. The creation of a large number of nanoparticles during the solidification of the SL prevented the formation of crystalline structure in the direction of the temperature gradient that is often observed in the SLs of metallic materials after DPF irradiation under the same conditions.

(a)

(b)

FIG. 20. Temperature distributions over the depth of the SL of a KP4-ODS steel specimen at various times (a) when it was heated by fluxes of fast deuterons and HP in the hard irradiation mode ($P_{FIS} = 5 \times 10^9$ W/cm^2, $\tau_{FIS} = 50$ ns; $P_{HP} = 10^8$ W/cm^2, $\tau_{HP} = 100$ ns) and (b) upon cooling.

b. Temperature distribution. Temperature estimates within the zone of the irradiated SL and their evolution in time were obtained by numerical modelling using the method described in Ref. 43. Figures 19 and 20 show curves of the variation of temperature with depth in the SL of KP4-ODS steel at different times obtained under the conditions presented in Table III. From these graphs, it can be concluded that in the thin SL (with thickness of about 50 nm) of the ODS steel specimens in the soft irradiation regime ($N = 2$ of with deuterium plasma and FIS: see Table III), the temperature may have reached values of about $T \approx 2500\,°C$, but no melting was observed. In these cases, erosion might have taken place for the solid solutions based on Fe and Cr that have lower melting temperatures. The mass loss on double irradiation was $\Delta m = 0.6$ mg.

In the case of the harsher irradiation regime with nine pulses, a melt was produced, as mentioned above and as can be seen from
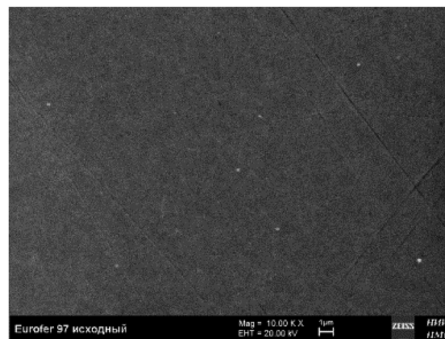

FIG. 21. Virgin Eurofer 97: 0.11 wt. % C; 9.0 wt. % Cr; 0.48 wt. % Mn; 1.1 wt. % W; 0.20 wt. % V; 0.07 wt. % Ta; 0.03 wt. % N; 0.005 wt. % P. Heat treatment was normalizing at 980 °C for 30 min plus tempering at 760 °C for 1.5 h.

Fig. 20. The appearance of a liquid phase in the presence of powerful streams of deuterium HP and FIS allowed partial or total dilution of the highly refractory oxide nanoparticles, depending on their sizes. Under these conditions, the radiation streams can produce in these particles quite high concentrations of point and linear defects.[44] This aided the transition into the melt of the oxide atoms at the border between the solid and liquid phases.

From the published data[45] on the binding energies for yttrium atoms (about 80 eV) and for oxygen atoms (36.6 eV) in the composition Y_2O_3 and from the value of ~134.5 eV for the energy of formation of Y_2O_3 from ions of yttrium (Y^{3+}) and oxygen (O^{2-}), it can be seen that the direct destruction of individual nanoparticles by fast high-energy deuterons ($E_D \geq 100$ keV) should be possible. An approximate estimate of the value of the diffusion transfer Y of the atoms of Y and O diluted in the liquid phase during the time t_0, for which this phase exists after a single pulse of the energy stream, can be obtained from the well-known relation

$$\chi^2 = 2Dt_0, \tag{5}$$
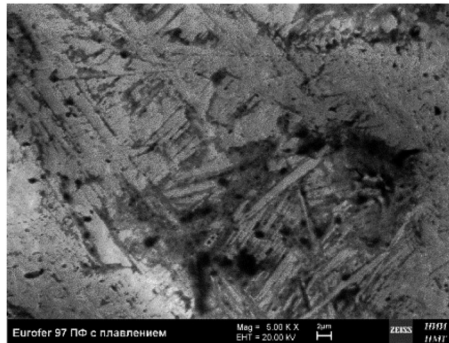
where D is the diffusion coefficient of an element in the metallic melt. Taking $t_0 \approx 100$ ns (see Fig. 20) and $D = 5 \times 10^{-5}$ cm^2/s,[46,47] one
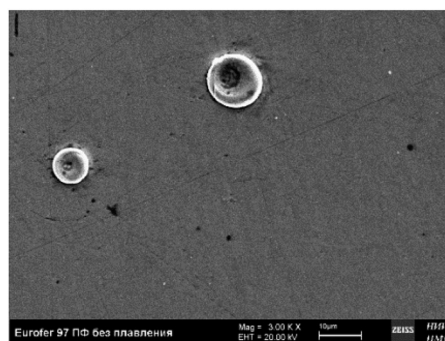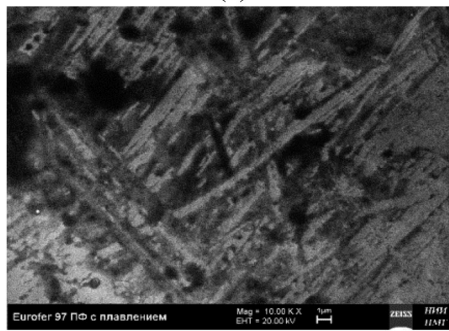

FIG. 22. Eurofer 97 after irradiation in the PF-6 device without melting of the SL (deuterium, $L = 18.3$ cm, $N = 7$ pulses). Round flat droplets of copper can be seen to appear as a consequence of the use of a DPF device with an oxygen-free copper anode.
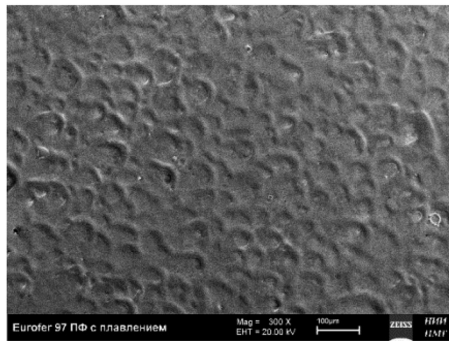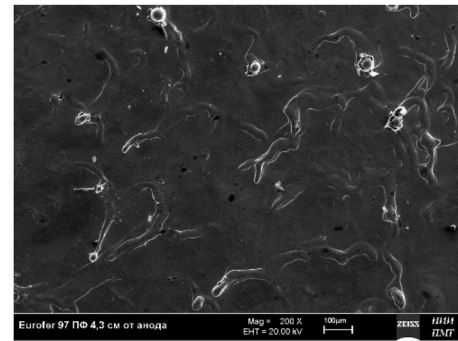
FIG. 23. Images at different magnifications of specimens of Eurofer 97 irradiated in the PF-6 device, showing surface melting (deuterium, distance $L = 13.8$ cm, $N = 7$ pulses).
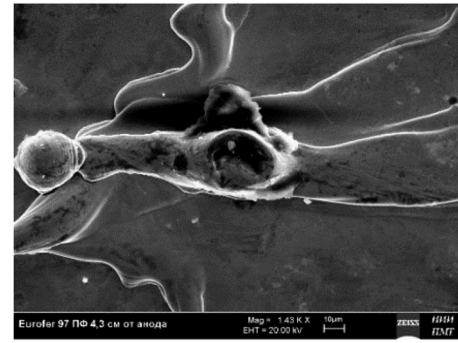

FIG. 24. Images of Eurofer 97 specimens irradiated at $P_{FIS} = 10^{12}$ W/cm^2 in the PF-6 device, showing strong melting of the surface (deuterium, $L = 4.3$ cm, 12 pulses).

obtains Y ≈ 32 nm. This estimate shows that in the harsh irradiation regime, the presence of the thermal component leads to a reduction in the heterogeneity of elemental concentrations through diffusion, the disappearance of the Cr-based solid melt, and the full dilution of small (<20 nm) reinforcing oxide nanoparticles (the melting temperature of the oxide Y_2O_3 is $T_{melt} \approx 2650$ °C[47]), all of which may have a deleterious effect upon ODS steel.
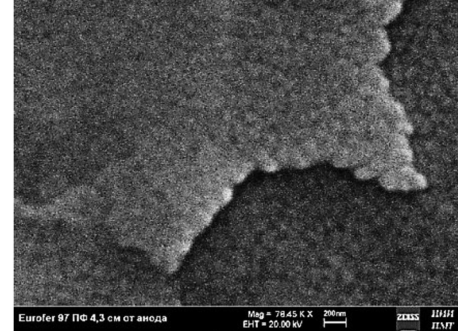
D. Irradiation of Eurofer 97 in the PF-6 device

In Figs. 21–24, SEM images are presented of specimens of Eurofer 97 steel in its virgin state and after irradiation in the PF-6 device at different distances from the anode: 18.3 cm; 13.8 cm; and 4.3 cm.

The corresponding power flux densities for HP and FIS, respectively, were 10^7 and 10^9 W/cm^2; 10^8 and 10^{10} W/cm^2; and 10^{10} and 10^{12} W/cm^2. In the first case, the surface acquires a predominantly cellular structure with the sizes of the cells being about 50 μm. A martensitic structure can be seen in particular near the "wave ridges."

Figure 24 shows the results of irradiation of a Eurofer 97 specimen by the highest power flux densities of HP and FIS.

The image in Fig. 24(c) reveals microcellular structures with sizes of about 200 nm. These are much smaller than the structures observed after irradiation at large distances, as shown in Fig. 23(a).

At very high magnification (i.e., >30 000), it can be seen that there are zones with martensitic-like structures where the martensitic pins decay into separate cells.

Figure 25 presents the diffraction patterns of the SLs of three Eurofer 97 specimens: virgin and irradiated at two distances: 13.8 cm and 4.3 cm.

The surface is strongly fused in this last case (see Fig. 24) and has a wave-like structure [Fig. 24(a)] that is dissimilar to the structures observed for irradiation distances 18.3 cm and 13.8 cm (Figs. 22 and 23). At the wave ridges, "coil-like configurations" can be seen [Fig. 24(b)].

E. Irradiation of V–10Ti–6Cr alloy and W specimens by laser radiation

Now let us examine the results of parallel irradiation of specimens of double-forged tungsten and of V–10Ti–6Cr by LR from a GOS-1001 laser working in the QS mode and by FIS in a DPF. These specimens were irradiated at about the same values of the power flux densities, namely, at $P \approx 10^{12}$ W/cm^2. It is interesting to compare the data taking into consideration the differences in the regions of absorption of different radiations and the underlying mechanisms.

Figure 26 presents SEM images of a V–10Ti–6Cr alloy target irradiated by LR from the Nd-glass laser in the QS mode with parameters $P_{LR} = 10^{12}$ W/cm^2, $\tau = 50$ ns, and $N = 8$. The picture that is seen in the case of laser irradiation of the surface is quite different from that in the case of DPF irradiation with the same power flux density of fast ions P_{FIS} (Fig. 24).

In the case of LR, in the central zone [CZ, i.e., the focal spot (see Fig. 9) and the area outlined by the rectangle in Fig. 26(a)], there was intense evaporation of the SL of the material, producing a deep crater
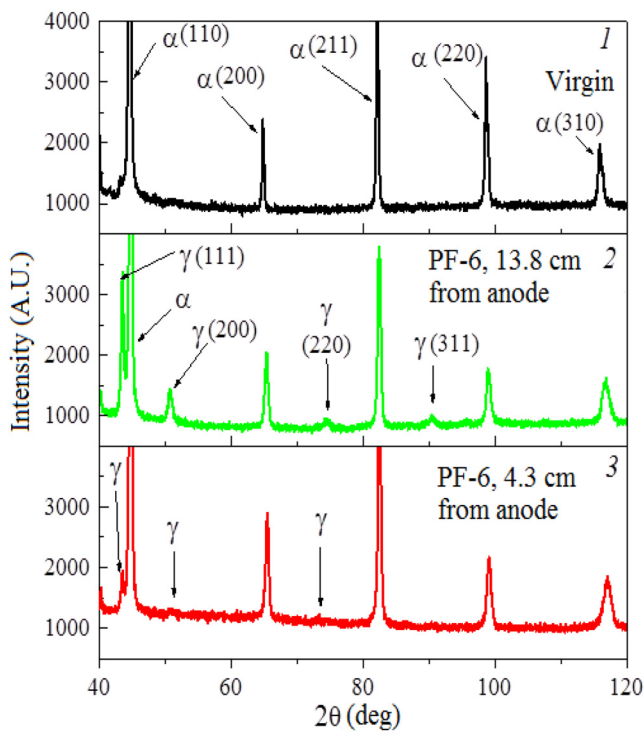

FIG. 25. X-ray diffraction patterns of the SL: virgin and irradiated at two different distances.

(so deep that its bottom is not visible). In the surrounding zone (ZTI), an indentation with a wave-like relief is visible, together with prolonged influxes and droplet structures. The roughness elements in this area are a few micrometers in height. In the zone in which the SL was heated by the laser-produced plasma, the melting is much less evident, with the roughness components being less than a 100 nm in height. In this irradiation regime, surface microcracks were absent. However, microparticles and droplets created during irradiation are clearly observed.

In our previous experiments[28] on double-folded W specimens subjected to laser irradiation in the Q-switched mode and to DPF irradiation at power flux densities of less than $P \sim 10^{11}$ W/cm^2 for both types of irradiation, transverse sections revealed a certain degree of stratification. This appeared as cracks and discontinuity flaws oriented parallel to the surface and situated at depths of about 100–200 μm. We observed the same effect at higher power flux densities $P_{FIS} \sim 10^{12}$ W/cm^2 ($N = 8$) following irradiation of W by FIS in the PF-1000U device and with the GOS-1001 laser also at $P_{DPF} \sim 10^{12}$ W/cm^2. These effects are more pronounced at the higher levels of irradiation. The depth of the noticeably damaged layer, in which disruption in the integrity of the material occurs, is about 300–400 μm in almost all the irradiation regimes studied. As in the previous case, the DPF device produced a greater degree of stratification than the laser.

tThe most plausible mechanism for the generation of stratification parallel to the specimen surface is connected with the generation of SWs and their action upon defects produced during manufacture of the material—very likely during its double forging in this case. The deeply located cracks oriented parallel to the specimen surface that were seen in SEM images of metallographic sections of W specimens irradiated at the highest power flux densities $P = 10^{12}$ W/cm^2 both for FIS in DPF and for LR were subjected to numerical modelling. This showed that the only explanation for the production of these cracks was the generation of SWs inside the bulk of the specimen.

The SW characteristics can be seen from the results of the numerical calculations (Fig. 27) based on the work in Ref. 48. These provided data on the pressure distribution with depth for both laser and FIS irradiation with the following parameters: $P = 10^{12}$ W/cm^2 with pulse durations $\tau \approx 50$ ns and 100 ns for LR and $\tau \approx 20$ ns and 40 ns for FIS in a DPF. The calculations showed that for similar characteristics of both energy streams, the amplitudes of the SWs generated by FIS in a DPF are about two times higher than those produced by LR (Table IV).

Table IV shows that an increase in the power flux density for LR from $P = 10^{11}$ W/cm^2 to $P = 10^{12}$ W/cm^2 led to an increase in the SW pressure from $p \approx 5$ GPa[28] to $p = 70$ GPa, and the same increase in the power flux density for FIS led to an increase in SW pressure from $p \approx 13$ GPa at $P = 10^{11}$ W/cm^2 to $p = 110$ GPa at 10^{12} W/cm^2. Again the dominant effect of the DPF compared with the laser is clearly observed here. This is a consequence of the much higher plasma density in the case of the DPF. This results from the difference in absorption mechanisms, in particular from the difference in the regions of absorption of the laser photons (by electrons at the critical laser plasma density of 10^{21} cm^{-3} for the Nd-glass laser: see Fig. 9) and of the fast ions (by ions of the target at the solid state density of 10^{23} cm^{-3}).

This is why the stratifications observed in metallographic sections of specimens after irradiation in a DPF are more pronounced than in the case of laser irradiation.
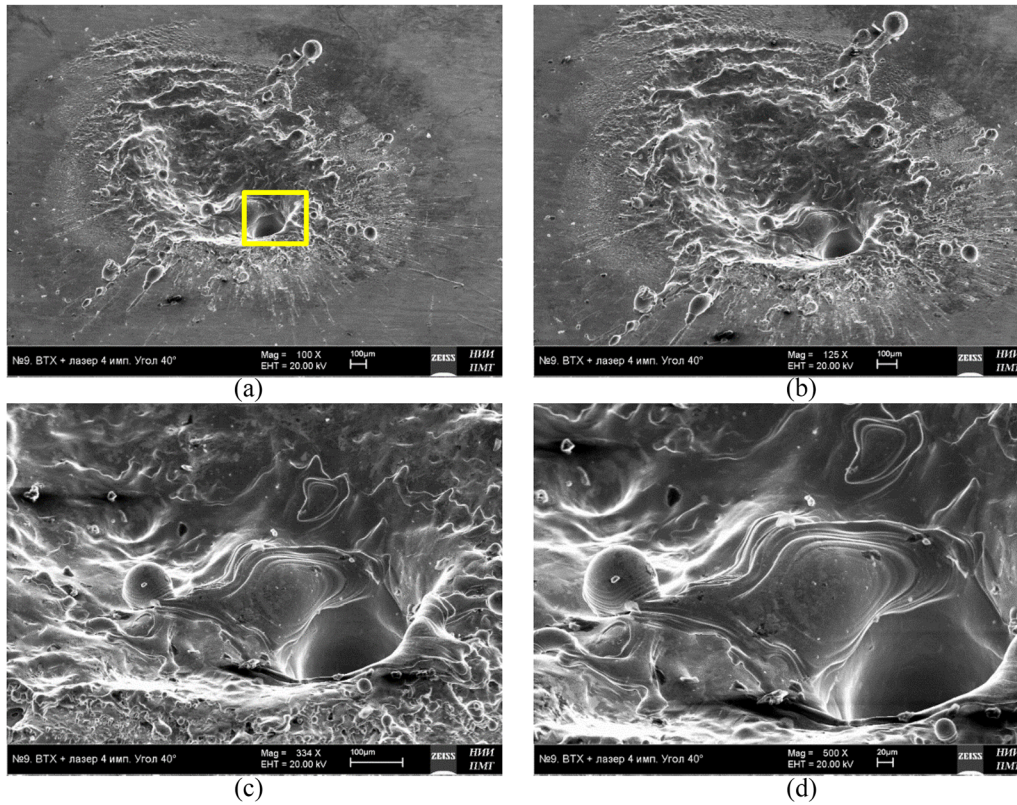
FIG. 26. SEM imagesof areas (different magnifications) of the surface of a V–10Ti–6Cr alloy target after irradiation by LR from a laser working in the QS mode with $P_{LR} = 10^{12}$ W/cm^2 and $\tau = 50$ ns: (a) and (b) zones of the focal spots (central zone, CZ: see Fig. 9) and of the thermal influence (ZTI) of a laser-produced flame; (c) and (d) CZ (focal spot) of the LR effect, with a crater [shown by the rectangle in (a)] of diameter less than 100 μm.
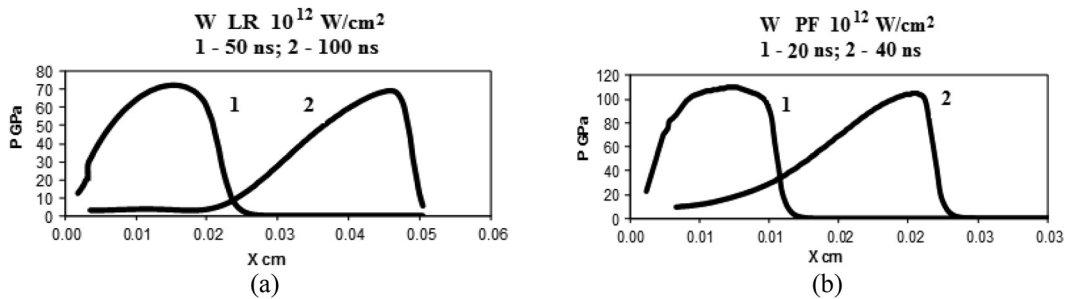

FIG. 27. Graphs of changes in SW pressure amplitude with depth after irradiation of W (a) by pulsed LR in the QS mode of operation with two pulse durations and (b) by plasma/ion streams in a DPF at two values of pulse duration and irradiation power flux densities $P = 10^{12}$ W/cm^2.

TABLE IV. Data on SW generation in W on irradiation by FIS and LR.

	P (W/cm^2)	Δt (ns)	d (mm)	L (μm)	T (eV)	p (GPa)
FIS	10^{12}	20	1	6	50	110
LR	10^{12}	50	0,2	3	180	70

VI. CONCLUSIONS AND RECOMMENDATIONS

(1) At the relatively low power flux densities of hot plasma (HP) and fast ion streams (FIS) (respectively $P \sim 10^5$–10^6 and 10^7–10^8 W/cm^2) generated in dense plasma focus (DPF) devices with short pulse durations ($\tau < 100$ ns), a roughening threshold of specimen surfaces is observed. Its value depends predominantly on the

number of DPF shots used during irradiation rather than from the power flux densities of the corresponding streams.

Therefore, to prevent strong roughening of plasma-facing components (PFCs) in nuclear fusion reactors (NFRs) with inertial plasma confinement (IPC), it is important to avoid exceeding the thresholds in the power flux densities of both streams ($P < 10^5$–10^6 for HP and 10^7–10^8 W/cm^2 for FIS) with short powerful pulses.

(2) Experiments with extremely high power flux densities $P \geq 10^9$–10^{10} for HP and 10^{11}–10^{12} W/cm^2 for FIS, which are higher than those to which PFCs in present-day NFRs with IPC ($P \leq 10^9$ W/cm^2) are subjected, have revealed well-developed gasdynamic motion of secondary plasma. Depending on the P values and pulse durations (assuming similar overall energy content), the ion streams and laser radiation in this regime will evaporate (ablate) from a target either a formidable mass of wall material at low temperature, which will generate high recoil momentum upon the PFC, or, in contrast, will evaporate a low mass of high-temperature material.

Therefore, the least suitable regimes for irradiation of PFCs with FIS and laser radiation (LR) are those with long pulses ($\tau > 100\ \mu s$) and intermediate power ($P \sim 10^8$–10^9 W/cm^2), where a large mass of cold materials may be evaporated and exert quite high momentum upon the PFCs.[28] Thus, one should not be afraid to have a relatively small chamber in an NFR with the IPC: a low mass loss and a weak momentum impact on the walls will result from the high power flux density.

(3) At the above-mentioned high values of P for FIS and LR, shock waves (SWs) may be generated inside the bulk material of PFCs. These SWs may reveal and even lead to strong growth of manufacturing defects in the material.

Hence, in the case of harsh irradiation regimes, materials with the minimal amount of manufacturing defects should be used for the first-wall elements.

(4) The concentration of hydrogen isotopes penetrating and subsequently confined in PFCs is reduced if the surface layers (SLs) of the latter have or acquire a convoluted morphology with a large area. This facilitates backward diffusion of gas into the NFR chamber.

Therefore, the surfaces of PFCs should not be polished, but rather should be prepared with a suitable surface morphology (which may be nanostructured). This prevents retention of radioactive substances (tritium fuel in particular) in the chamber walls.

(5) Mass loss from some types of ceramics due to irradiation by high-power HP and FIS is about the same or even less compared with that from metals. This results from the very small time intervals of PFC irradiation in NFRs with IPC ($\tau \leq 0.01$–$1.0\ \mu s$), which are much shorter than the characteristic heat conduction time scale (10–100 μs).

Thus, the thermal conductivity of PFC materials in NFRs with IPC does not play an important role in the irradiation and damage processes.

Therefore, those types of ceramics that have demonstrated good radiation resistance can be considered suitable for first-wall components.

(6) The harshest short-pulsed regimes of PFC irradiation can be modeled not only by DPF devices but also by lasers operating in the Q-switched mode. However, in this case, the irradiation parameters (e.g., SW amplitudes) are smaller than those for FIS, because of the different zones of action and underlying mechanisms of LR and FIS absorption. It also needs to be taken into account that the SL morphology after irradiation by LR is different from that after the irradiation by FIS.

ACKNOWLEDGMENTS

REFERENCES

[1]See http://www.iter.org/ for information about the problem of radiation resistance of materials in the context of nuclear fusion with magnetic plasma confinement.

[2]S. Brezinsek, J. W. Coenen, T. Schwarz-Selinger, K. Schmid, A. Kirschner et al. (WP PFC Contributors), Nucl. Fusion **57**, 116041 (2017).

[3]I. E.Garkusha, I. Landman, J. Linke, V. A. Makhlaj, A. V. Medvedev et al., "Performance of deformed tungsten under ELM-like plasma exposures in QSPA Kh-50," J. Nucl. Mater. **415**, S65–S69 (2011).

[4]N. Klimov, V. Podkovyrov, A. Zhitlukhin, and D. Kovalenko, "Experimental study of PFCs erosion under ITER-like transient loads at plasma gun facility QSPA," J. Nucl. Mater. **390-391**, 721–726 (2009).

[5]P. Fiflis, T. W. Morgan, S. Brons, G. G. Van Eden, M. A. Van Den Berg et al, "Performance of the lithium metal infused trenches in the magnum PSI linear plasma simulator," Nucl. Fusion **55**, 113004 (2015).

[6]N. Almousa, L. Winfrey, J. Gilligan, and M. Bourham, "Radiative heat transport through vapor plasma for fusion heat flux studies and electrothermal plasma sources applications," J. Nucl. Energy Sci. Power Generat. Technol. **3**, 1000116 (2014).

[7]Th. Loewenhoff, T. Hirai, S. Keusemann, J. Linke, G. Pintsuk et al., "Experimental simulation of edge localized modes using focused electron beams—Features of a circular load pattern," J. Nucl. Mater. **415**(1), S51–S54 (2011).

[8]E. V.Morozov, A. S. Demin, V. N. Pimenov, V. A. Gribkov, V. V. Roshchupkin et al., "Features of damage and structural changes in the surface layer of tungsten under the pulsed action of laser radiation, ion and plasma fluxes," Phys. Chem. Mater. Treatment. **4**, 5–18 (2017) (in Russian).

[9]See https://lasers.llnl.gov/ for information about nuclear fusion reactors with inertial plasma confinement.

[10]See http://www.sandia.gov/z-machine/ for information about nuclear fusion reactors with inertial plasma confinement.

[11]T. J. Tanaka, G. A. Rochau, R. R. Peterson, and C. L. Olson, "Testing IFE materials on Z," J. Nucl. Mater. **347**, 244–254 (2005).

[12]J. F. Latkowski, R. P. Abbott, R. C. Schmitt, and B. K. Bell, "Effect of multi-shot X-ray exposures in IFE armor materials," J. Nucl. Mater. **347**, 255–265 (2005).

[13]A. M. Stoneham, J. R. Matthews, and I. J. Ford, "Innovative materials for fusion power plant structures: Separating functions," J. Phys.: Condens. Matter **16**, s2597–s2621 (2004).

[14]Handbook of Physical Quantities, edited by I. S. Grigoriev, E. Z. Meilikhov, and A. A. Radzig (CRC Press, Boca Raton, 1997), 1548 p., ISBN: 9780849328619, CAT No. 2861.

[15]T. Renk, "Long-term exposure of tungsten and other materials to intense pulsed ion beams, beam applications and initiatives," in *Sandia National Laboratories, Transient Loading Workshop (Proceedings of Transient Loading Workshop, November 15–17, 2005)* (Institute of Plasma Physics and Laser Microfusion, Warsaw, Poland, 2005).

[16]M. Fujitsuka, H. Shinno, T. Tanabe, and H. Shiraishi, "Thermal shock experiments for carbon materials by electron beams," J. Nucl. Mater. **179-181**(part A), 189–192 (1991).

[17]M. A. Orlova, O. A. Kost, V. A. Gribkov, I. G. Gazaryan, A. V. Egorov *et al.*, "Enzyme activation and inactivation induced by low doses of irradiation," Appl. Biochem. Biotechnol. **88**, 243–255 (2000).

[18]O. A.Troshina, D. A. Callahan, D. T. Casey, P. M. Celliers, C. Cerjan *et al*, "Fuel gain exceeding unity in an inertially confined fusion implosion," Nature **506**, 343–348 (2014).

[19]A. Bernard, H. Bruzzone, P. Choi, H. Chuaqui, V. Gribkov *et al.*, "Scientific status of plasma focus research," J. Moscow Phys. Soc. **8**, 93–170 (1998).

[20]V. A. Gribkov, L. Karpinski, P. Strzyzewski, M. Scholz, and A. Dubrovskij, "New efficient low-energy dense plasma focus in IPPLM," Czech J. Phys. **54**(Suppl. C), 191–197 (2004).

[21]M. Scholz, R. Miklaszewski, V. A. Gribkov, and F. Mezzetti, "PF-1000 device," Nukleonika **45**(3), 155–158 (2000).

[22]V. A. Gribkov, I. V. Borovitskaya, A. S. Demin, E. V. Morozov, S. A. Maslyaev *et al.*, "The Vikhr plasma focus device for diagnosing the radiation-thermal resistance of materials intended for thermonuclear energy and aerospace engineering," Instrum. Exp. Techn. **63**(1), 68–76 (2020).

[23]V. Shirokova, T. Laas, A. Ainsaar, J. Priimets, Ü. Ugaste *et al.*, "Comparison of damages in tungsten and tungsten doped with lanthanum-oxide exposed to dense deuterium plasma shots," J. Nucl. Mater. **435**, 181–188 (2013).

[24]V. A. Gribkov, M. Paduch, E. Zielinska, A. S. Demin, E. V. Demina *et al.*, "Comparative analysis of damageability produced by powerful pulsed ion/plasma streams and laser radiation on the plasma-facing W samples," Radiat. Phys. Chem. **150**, 20–29 (2018).

[25]V. A. Gribkov, A. S. Demin, N. A. Epifanov, E. E. Kazilin, S. V. Latyshev *et al*, "Damageability of the Al_2O_3 oxide coating on the aluminum substrate by pulsed beam plasma and laser radiation," Inorg. Mater. Appl. Res. **10**, 339–346 (2019).

[26]T. Laas, K. Laas, J. Paju, J. Priimets, S. Tõkke *et al*, "Behavior of tungsten alloy with iron and nickel under repeated high temperature plasma pulses," Fusion Eng. Des. **151**, 111408 (2020).

[27]E. V. Demina, V. A. Gribkov, M. D. Prusakova, V. N. Pimenov, V. P. Sirotinkin *et al.*, "Behavior of the 16%Cr ODS ferritic steel intended for nuclear fusion power industry after tests in the conditions of irradiation in the Dense Plasma Focus facility PF-1000U," J. Phys.: Conf. Ser. **1347**, 012069 (2019).

[28]V. A. Gribkov, E. V. Demina, E. E. Kazilin, S. V. Latyshev, S. A. Maslyaev *et al.*, "Testing of materials perspective for nuclear fusion reactors with inertial plasma confinement by Plasma Focus and laser devices," J. Phys.: Conf. Ser. **1347**(1), 012071 (2019).

[29]G. Pintsuk, "Tungsten as a plasma-facing material," in *Comprehensive Nuclear Materials*, edited by R. J. M. Konings (Elsevier, Amsterdam, The Netherlands, 2012).

[30]Ya. B. Zel'dovich and Yu. P. Raizer, *Physics of Shock Waves and High-Temperature Hydrodynamic Phenomena* (Academic, New York, 1966), Vols. 1 and 2.

[31]V. A. Gribkov, S. V. Latyshev, S. A. Maslyaev, and V. N. Pimenov, "Numerical modeling of interaction of pulsed streams of energy with material in the dense plasma focus devices," Phys. Chem. Mater. Treatment. **6**, 16–22 (2011) (in Russian).

[32]S. V. Latyshev, V. A. Gribkov, S. A. Maslyaev, V. N. Pimenov, M. Paduch *et al.*, "Generation of shock waves in materials science experiments with dense plasma focus device," Inorg. Mater.: Appl. Res. **6**(2), 91–95 (2015).

[33]Z. Zielinska, *Advanced Materials for Future Nuclear Plants* (Oak Ridge National Laboratory, Oak Ridge, 2007); [*TN Fission Energy Workshop: Opportunities for Fundamental Research and Breakthrough in Fission Global Climate and Energy Project* (Massachusetts Institute of Technology, Cambridge, MA, 2007), pp. 1–29].

[34]K. L. Murty and I. Charit, "Structural materials for Gen-IV nuclear reactors: Challenges and opportunities," J. Nucl. Mater. **383**(1-2), 189–195 (2008).

[35]C. R. F. Azevedo, "Selection of fuel cladding material for nuclear fission reactors," Eng. Failure Anal. **18**(8), 1943–1962 (2011).

[36]P. Yvon and F. Carré, "Structural materials challenges for advanced reactor systems," J. Nucl. Mater. **385**(2), 217–222 (2009).

[37]S. Ukai and M. Fujiwara, "Perspective of ODS alloys application in nuclear environments," J. Nucl. Mater. **307-311**(Part 1), 749–757 (2002).

[38]R. Kasada, N. Toda, K. Yutani, H. S. Cho, H. Kishimoto *et al.*, "Pre- and post-deformation microstructures of oxide dispersion strengthened ferritic steels," J. Nucl. Mater. **367-370**(Part A), 222–228 (2007).

[39]R. Kimura, A. Möslang, M. Schirra, P. Schlossmacher, and M. Klimenkov, "Mechanical and microstructural properties of a hipped RAFM ODS-steel," J. Nucl. Mater. **307-311**, 769–772 (2002).

[40]R. L. Klueh, P. J. Maziasz, I. S. Kim, L. Heatherly, D. T. Hoelzer *et al*, "Tensile and creep properties of an oxide dispersion-strengthened ferritic steel," J. Nucl. Mater. **307-311**, 773–777 (2002).

[41]D. A. McClintock, M. A. Sokolov, D. T. Hoelzer, and R. K. Nanstad, "Mechanical properties of irradiated ODS-EUROFER and nanocluster strengthened 14YWT," J. Nucl. Mater. **392**, 353–359 (2009).

[42]N. V. Luzginova, J. Rensman, P. Pierick, and J. B. J. Hegeman, "Irradiation response of ODS Eurofer97 steel," J. Nucl. Mater. **428**, 192–196 (2012).

[43]S. A. Maslyaev, "Thermal effects during pulsed irradiation of materials in the plasma focus device," Adv. Mater. **5**, 47–55 (2007) (in Russian).

[44]G. G. Bondarenko, *Radiation Physics, Structure and Strength of Solids* (Pilot LZ, Moscow, 2016) (in Russian).

[45]L. P. Putilov, A. N. Varaksin, and V. I. Tsidilkovski, "Defect formation and water incorporation in Y_2O_3," J. Phys. Chem. Solids **72**, 1090–1095 (2011).

[46]L. I. Larikov and V. I. Isaichev, *Diffusion in Metals and Alloys* (Naukova Dumka, Handbook, Kiev, 1989), 510 p. (in Russian).

[47]A. A. Vostryakov, E. A. Pastukhov, N. I. Sidorov, and I. S. Sipatov, "Diffusion in Ta, Nb, and Zr melts," Butlerov Commun. **30**(5), 20–24 (2012) (in Russian).

[48]V. A. Gribkov, S. V. Latyshev, S. A. Maslyaev, and V. N. Pimenov, "Numerical simulation of the interaction of pulsed energy fluxes with material in Plasma focus device," Phys. Chem. Mater. Treatment. **6**, 16–22 (2011) (in Russian).